A bond model for ribbed bars based on concrete confinement

Joop A. den Uijl, Agnieszka J. Bigaj
Stevin Laboratory, Delft University of Technology

A new bond model for ribbed bars embedded in concrete has been developed. The model is based on the confining capacity of the concrete surrounding the bar. This confinement capacity is evaluated with the help of a thick-walled-cylinder model, with which the relation between the radial displacement and the radial compressive stress at the steel-to-concrete interface is described. Next, the slip of the ribbed bar is linked to the radial displacement of the interface, treating the two modes of bond failure, splitting of the cover and pull-out of the bar, in a different way.
The model takes into account the effect of concrete softening in tension and of bar contraction connected to yielding. It has been tuned and verified on the basis of a broad range of experimental results.

Keywords: **bond, ribbed bars, concrete confinement, splitting failure, pull-out failure, concrete softening, Poisson effect, steel yielding**

1 Introduction

The degree of confinement of a ribbed bar embedded in concrete not only affects the magnitude of the ultimate bond stress but also the bond stress-slip relation. This has been recognized in MC90 (CEB-FIP Model Code 1990), where both characteristics have been defined as a function of the bond failure mode: splitting ("unconfined concrete") or pull-out ("confined concrete") and the bond conditions ("good" or "all other cases"). Hence, the bond stress-slip relation has not been defined as a continuous function of the concrete cover, but it has only been given for two discrete values of the cover, viz. for unconfined concrete $c/d_s = 1$[1] (requiring a minimum amount of transverse reinforcement) and for confined concrete $c/d_s = 5$.
However, for a more refined analysis of phenomena in which bond plays a dominant role a bond stress-slip relation is required that more accurately takes into account the concrete confining capacity. For example the length of a plastic hinge, which is of importance for the rotational capacity of reinforced concrete members, depends among other things on the force transfer from reinforcement to concrete between subsequent bending cracks (Bigaj and Walraven 1996).
The importance of the concrete confining capacity for the bond resistance of a ribbed bar directly follows from the analysis of the force transfer between the bar and the surrounding concrete. The radial components of the concentrated forces, that radiate from the bar into the concrete, are

[1] Symbols that are used once are explained in de text, the others are given at the back.

equilibrated by circumferential tensile forces in the concrete and by any additional confinement, such as transverse reinforcement and external forces. This confining action determines the mode of bond failure and other specific bond characteristics.
In the bond model given hereafter the concrete confining capacity is used as a starting point to describe the bond behaviour of a ribbed bar embedded in concrete. Here only the confinement delivered by the surrounding concrete is considered. This confining capacity is analytically estimated taking into account the softening behaviour of concrete loaded in tension. It is expressed by the relation between the radial stress and the radial displacement of the bar-to-concrete interface. For the transition from this relation to a bond stress-slip relation the ribbed bar is conceived as a smooth conical bar transferring the bond stress through dry friction to the concrete. The "bar-to-concrete interface" is further denoted as "interface".

2 Concrete confinement model

To describe the resistance of the concrete cover against splitting due to bond the model of a thick-walled-cylinder is used, in which the radial component of the bond action makes equilibrium with the circumferential tensile stresses across the cylinder wall. As long as these hoop stresses remain below the tensile strength a linear elastic stress state is present, for which analytical expressions are available. When the circumferential stress reaches the tensile strength one or more radial cracks start to grow and the response of the concrete to the internal pressure becomes non-linear. For this stage Tepfers (1979) considered a lower and an upper bound solution. The lower bound was given by assuming that in the cracked part of the cylinder the circumferential tensile stresses are equal to zero and that the uncracked part behaves linear elastically. The upper bound followed from the assumption of a purely plastic material behaviour, which yields a uniformly distributed circumferential tensile stress equal to the tensile strength. A more refined approximation for the non-linear state was developed by Van der Veen (1990), extending Tepfers' cracked-elastic model by taking into account the softening behaviour of concrete. The splitting resistance found with this approach falls between Tepfers' lower and upper bounds and shows good resemblance with experimental results.
The aforesaid models only deal with the concrete stresses around a bar, which suffices to establish a criterion for bond splitting failure. In the present approach, however, the bond stress is considered as a function of the concrete response to the radial displacement of the interface. Therefore, the concrete deformations involved have to be considered as well.

2.1 *Uncracked stage (stage I)*

The response of a thick-walled-cylinder to an internal pressure can be subdivided into three stages: the uncracked, partly cracked and entirely cracked stage, respectively.
In the uncracked stage a linear elastic behaviour of the cylinder can be assumed, for which the stresses and deformations have been given by Timoshenko (1976):

$$\sigma_{r,r} = \frac{r_i^2 \sigma_{r,r_i}}{r_e^2 - r_i^2}\left(1 - \frac{r_e^2}{r^2}\right) \tag{2.1}$$

$$\sigma_{t,r} = \frac{r_i^2 \sigma_{r,r_i}}{r_e^2 - r_i^2}\left(1 + \frac{r_e^2}{r^2}\right) \tag{2.2}$$

$$u_{r,r_i} = \frac{r_i \sigma_{r,r_i}}{E_c}\left(\frac{r_e^2 + r_i^2}{r_e^2 - r_i^2} + v_c\right) \tag{2.3}$$

with $r_i = r_s = \frac{d_s}{2}$ and $r_e = c_1 = c + r_s = c + \frac{d_s}{2}$

Normalizing the radial displacement of the interface to the bar radius yields a dimensionless quantity, which is further denoted as the radial strain at the interface.

2.2 *Partly cracked stage (stage II)*

To find the $\sigma_r - \varepsilon_r$-relationship at the interface in the second stage the cylinder is subdivided into a cracked part and an uncracked part (Fig. 2.1). At the crack front $r = r_{cr}$ the circumferential stress is – per definition – equal to the tensile strength. Substitution of $\sigma_{t,r} = f_{ct}$ and $r = r_{cr}$ into eq. (2.2) and taking $r_i = r_{cr}$ and $r_e = c_1$ yields for the radial stress at the crack front:

$$\sigma_{r,r_{cr}} = f_{ct}\frac{c_1^2 - r_{cr}^2}{c_1^2 + r_{cr}^2} = f_{ct} C_1 \tag{2.4}$$

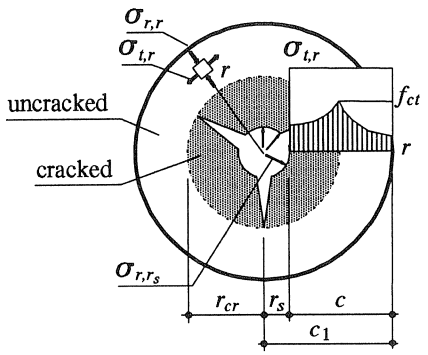

Fig. 2.1. Partly cracked thick-walled-cylinder.

Hence, at the interface the uncracked cylinder contributes to the radial stress:

$$\sigma_{r,r_s}^{LE} = \frac{r_{cr}}{r_s} = \sigma_{r,r_{cr}} = \frac{r_{cr}}{r_s} f_{ct} c_1 \tag{2.5}$$

The superscripts *LE* (linear elastic) and *NL* (non linear) refer to the contribution of the uncracked part and the cracked part, respectively.

Substitution of eq. (2.4) into eq. (2.3) and taking $\frac{f_{ct}}{E_c} = \varepsilon_{cr}$ gives:

$$u_{r,r_{cr}} = r_{cr}\varepsilon_{cr}\left(1 + v_c\frac{c_1^2 - r_{cr}^2}{c_1^2 + r_{cr}^2}\right) = r_{cr}\varepsilon_{cr}(1 + v_c C_1) \tag{2.6}$$

Thus, the uncracked cylinder contributes to the radial strain at the interface:

$$\sigma_{r,r_s}^{LE} = \frac{r_{cr}}{r_s}\varepsilon_{cr}(1 + v_c C_1) \tag{2.7}$$

To estimate the contribution of the cracked cylinder to the radial stress and strain at the interface the softening behaviour of concrete loaded in tension is taken into account by applying Hillerborg's (1983) fictitious crack model (FCM). A bi-linear softening relation as proposed by Roelfstra and Wittmann (1986) is chosen:

$$\frac{\sigma_t}{f_{ct}} = a\frac{w_t}{w_0} + b \tag{2.8}$$

Expressing the constants a and b in the normalized coordinates α and β of the intersection point (Fig. 2.2) yields for the first and second branch, respectively:

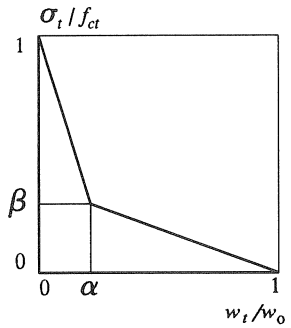

Fig. 2.2. Bi-linear softening diagram for concrete in tension.

$$\frac{\sigma_t}{f_{ct}} = -\frac{1-\beta}{\alpha}\frac{w_t}{w_0} + 1 \tag{2.9}$$

$$\frac{\sigma_t}{f_{ct}} = \frac{\beta}{1-\alpha}\frac{w_t}{w_0} + \frac{\beta}{1-\alpha} \tag{2.10}$$

The fracture energy G_f and the characteristic length l_{ch}, which is a measure for the brittleness, can be expressed in the same coordinates:

$$G_f = 0.5(\alpha + \beta) w_0 f_{ct} \tag{2.11}$$

$$l_{ch} = \frac{G_f E_c}{f_{ct}^2} \tag{2.12}$$

For normal density concrete – both for NSC and HSC – the localized deformation at failure w_0 is assumed to be 0.2 mm, the value of α is set to 0.14, while the value of β is linked to the concrete strength according to:

$$\begin{aligned} &\text{for } f_c < 30 \text{ MPa} \quad && \beta = 0.25 \\ &\text{for } f_c \geq 30 \text{ MPa} \quad && \beta = 0.25 - 0.015\,(f_c - 30) \end{aligned} \tag{2.13}$$

These values were derived from experimental results reported by Roelfstra and Wittmann (1986) for NSC and Walraven et al. (1993) for HSC.
By rewriting eq. (2.8) the fictitious crack width can be expressed as:

$$w_t = \frac{w_0}{a}\left(\frac{\sigma_t}{f_{ct}} - b\right) \tag{2.14}$$

The total elongation of a circular fibre with radius r consists of the total width of the fictitious cracks and the elastic deformation of the concrete between those cracks. Neglecting the influence of the radial stress on the tangential deformation, the fibre elongation can be written as:

$$\Delta_{t,r} = 2\pi r \varepsilon_{t,r} + n\frac{w_0}{a}\left(\frac{\sigma_{t,r}}{f_{ct}} - b\right) \tag{2.15}$$

n being the number of fictitious cracks.
To establish the distribution of the circumferential tensile stresses across the wall of the cracked cylinder, in his first modelling step Van der Veen regards the concrete segments between the cracks to be stress free and considers the rigid body movement of these segments, which results in a constant crack width across the wall, shown in Fig. 2.3 (left). In reality, however, these cracks are partly

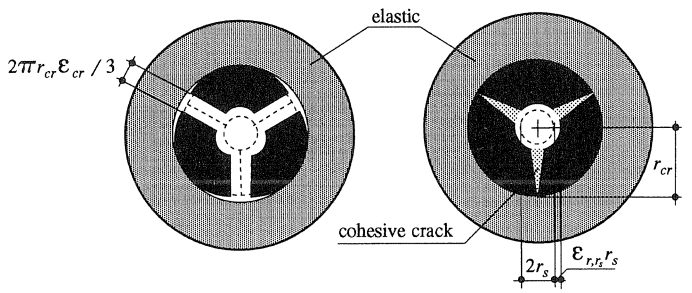

Fig. 2.3. Rigid body movement of segments in cracked part of cylinder (left) and deformed segments due to tangential tensile stresses transmitted by cracks (right) after Van der Veen (1990).

closed by circumferential tensile stresses as long as the width of the individual cracks is smaller than w_0. This is included in the final model, as shown in Fig. 2.3 (right). At the crack front, where the circumferential stress equals the tensile strength, the cracks are entirely closed and the total fibre elongation is only caused by elastic deformation. Neglecting the Poisson effect this deformation equals $2\pi r_{cr}\varepsilon_{cr}$, thus:

$$2\pi r_{cr}\varepsilon_{cr} = 2\pi r\varepsilon_{t,r} + n\frac{w_0}{a}\left(\frac{\sigma_{t,r}}{f_{ct}} - b\right) \tag{2.16}$$

which becomes after rewriting:

$$\frac{\sigma_{t,r}}{f_{ct}} = a\frac{2\pi\varepsilon_{cr}}{nw_0}\left(r_{cr} - \frac{\varepsilon_{t,r}}{\varepsilon_{cr}}r\right) + b = aC_2\left(r_{cr} - \frac{\varepsilon_{t,r}}{\varepsilon_{cr}}r\right) + b \tag{2.17}$$

The radial stresses which make equilibrium with the circumferential tensile stresses in the cracked part of the cylinder follow from:

$$\sigma^{NL}_{r,r} = \frac{1}{r}\int_{r}^{r_{cr}} \sigma_{t,r}\ \mathrm{d}r \tag{2.18}$$

To simplify the integration operation, the ratio $\varepsilon_{t,r}/\varepsilon_{cr}$ in eq. (2.17) is put equal to 1, which involves a certain overestimation of the circumferential strain in the cracked cylinder. On the other hand, this strain was underestimated by neglecting the Poisson effect at the crack front. Hence, both effects partly neutralize each other. Substitution of eq. (2.17) into eq. (2.18) and integration of the latter yields:

$$\frac{\sigma^{NL}_{r,r}}{f_{ct}} = \frac{aC_2 r}{2}\left(\frac{r_{cr}}{r} - 1\right)^2 + b\left(\frac{r_{cr}}{r} - 1\right) \tag{2.19}$$

Substitution of $r = r_s$ into eq. (2.19) gives the contribution of the cracked cylinder to the radial stress at the interface:

$$\frac{\sigma^{NL}_{r,r_s}}{f_{ct}} = \frac{aC_2 r_s}{2}\left(\frac{r_{cr}}{r} - 1\right)^2 + b\left(\frac{r_{cr}}{r} - 1\right) \tag{2.20}$$

Now the confining stress of the entire cylinder in the partly cracked stage (stage II) is given by the sum of eq. (2.5) and eq. (2.20):

$$\frac{\sigma^{II}_{r,r_s}}{f_{ct}} = \frac{\sigma^{LE}_{r,r_s}}{f_{ct}} + \frac{\sigma^{NL}_{r,r_s}}{f_{ct}} \tag{2.21}$$

The superscripts I, II and III refer to the three stages of behaviour of the cylinder: uncracked, partly cracked and entirely cracked, respectievly.

The radial deformation of the cracked cylinder is evaluated assuming the Poisson effect to play a minor role compared to the influence of the fictitious cracks. Therefore the change of the wall thickness of the cracked cylinder can be written as:

$$\Delta c_{cr}^{NL} = \int_{r_s}^{r_{cr}} \frac{\sigma_{r,r}^{II}}{E_c} dr = \varepsilon_{cr} \int_{r_s}^{r_{cr}} \frac{\sigma_{r,r}^{II}}{f_{ct}} dr = \varepsilon_{cr} \int_{r_s}^{r_{cr}} \frac{\sigma_{r,r}^{LE}}{f_{ct}} dr + \varepsilon_{cr} \int_{r_s}^{r_{cr}} \frac{\sigma_{r,r}^{NL}}{f_{ct}} dr \tag{2.22}$$

with $\frac{f_{ct}}{E_c} = \varepsilon_{cr}$

From eq. (2.4) the uncracked cylinder's contribution to the radial stress in the cracked cylinder is known:

$$\frac{\sigma_{r,r}^{LE}}{f_{ct}} = \frac{r_{cr}}{r} \frac{\sigma_{r,r_{cr}}}{f_{ct}} = \frac{r_{cr}}{r} C_1 \tag{2.23}$$

and the contribution of the circumferential tensile stresses in the cracked cylinder to the radial stress is given by eq. (2.19). Substitution of eq. (2.4) and eq. (2.19) into eq. (2.22) and rewriting yields: with:

$$\Delta c_{cr}^{NL} = \Delta c_{cr,1} + \Delta c_{cr,2} \tag{2.24}$$

$$\Delta c_{cr,1} = \varepsilon_{cr} C_1 \int_{r_s}^{r_{cr}} \frac{r_{cr}}{r} dr = \varepsilon_{cr} C_1 r_{cr} \ln\left(\frac{r_{cr}}{r_s}\right) \tag{2.25}$$

and:

$$\Delta c_{cr,2} = \varepsilon_{cr} \int_{r_s}^{r_{cr}} \frac{a C_2 r}{2} \left(\frac{r_{cr}}{r} - 1\right)^2 dr + \varepsilon_{cr} \int_{r_s}^{r_{cr}} b \left(\frac{r_{cr}}{r} - 1\right) dr =$$

$$= \frac{\varepsilon_{cr} a C_2}{4} \left(2 r_{cr}^2 \ln\left(\frac{r_{cr}}{r_s}\right) - 4 r_{cr}(r_{cr} - r_s) + (r_{cr}^2 - r_s^2)\right) + \varepsilon_{cr} b \left(r_{cr} \ln\left(\frac{r_{cr}}{r}\right) - (r_{cr} - r_s)\right) \tag{2.26}$$

Now, the radial strain at the interface due to the change of the wall thickness of the cracked cylinder follows from:

$$\varepsilon_{r,r_s}^{NL} = \frac{\Delta c_{cr}^{NL}}{r_s} = \frac{\Delta c_{cr,1}}{r_s} + \frac{\Delta c_{cr,2}}{r_s} \tag{2.27}$$

The total radial strain at the interface is the sum of the strain due to the deformation of the uncracked part of the cylinder and the aforementioned change in wall thickness of the cracked part of the cylinder, as given by eq. (2.7) and (2.27), respectively:

$$\varepsilon_{r,r_s}^{II} = \varepsilon_{r,r_s}^{LE} + \varepsilon_{r,r_s}^{NL} \tag{2.28}$$

2.3 *Entirely cracked stage (stage III)*

Up to now the radial stress-strain behaviour that occurs in the first two stages, during which radial cracks are initiated and driven through the entire wall of the cylinder, has been derived. In the third stage these cracks become wider and the confining action of the concrete diminishes as a consequence of the softening behaviour. The derivation of the radial stress-strain relation for this stage is analogous to that for the cracked part of the cylinder in the second stage. First, the circumferential tensile stress is estimated assuming the total elongation of the fibres across the cylinder wall to be constant ($\Delta_{t,r} = \Delta_{tot}$) and the tangential strain $\varepsilon_{t,r}$ to be equal to the fracture strain ε_{cr}. Substituting these values into eq. (2.15) and rewriting yields:

$$\frac{\sigma_{t,r}}{f_{ct}} = a\left(\frac{\Delta_{tot}}{nw_0} - \frac{2\pi\varepsilon_{cr}}{nw_0}\right) + b = a(C_3 + C_2 r) + b \tag{2.29}$$

Next, the radial stress is found after substitution of eq. (2.29) into eq. (2.18) and integration between r and c_1:

$$\frac{\sigma_{r,r}}{f_{ct}} = (aC_3 + b)\left(\frac{C_1}{r} - 1\right) - \frac{aC_2 r}{2}\left(\left(\frac{c_1}{r}\right)^2 - 1\right) \tag{2.30}$$

Substituting $r = r_s$ in eq. (2.30) yields the radial stress acting at the interface:

$$\frac{\sigma^{III}_{r,r_s}}{f_{ct}} = (aC_3 + b)\left(\frac{C_1}{r_s} - 1\right) - \frac{aC_2 r_s}{2}\left(\left(\frac{c_1}{r_s}\right)^2 - 1\right) \tag{2.31}$$

The radial strain at the interface is derived from the radial displacement, which consist of two parts: the rigid body movement (RBM) equal to the radial displacement of the outer fibre and the change of the wall thickness (Δc):

$$\varepsilon^{III}_{r,r_s} = \varepsilon^{RBM}_{r,r_s} + \varepsilon^{\Delta c}_{r,r_s} \tag{2.32}$$

The strain due to the rigid body movement can be written as:

$$\varepsilon^{RBM}_{r,r_s} = \frac{\Delta r_s}{r_s} = \frac{\Delta_{tot}}{2\pi r_s} = C_3\frac{nw_0}{2\pi r_s} \tag{2.33}$$

The strain connected with the wall thickness change is obtained by integrating eq. (2.30) over the cylinder wall and dividing it by the elastic modulus and the bar radius:

$$\varepsilon^{\Delta c}_{r,r_s} = \frac{\Delta c}{r_s} = \frac{1}{r_s}\int_{r_s}^{c_1}\frac{\sigma_{r,r}}{E_c}dr = \frac{\varepsilon_{cr}}{r_s}\left(a(C_3 + b)\int_{r_s}^{c_1}\left(\frac{c_1}{r} - 1\right)dr - \frac{aC_2}{2}\int_{r_s}^{c_1}\left(\frac{c_1^2}{r} - r\right)dr\right) =$$

$$= \varepsilon_{cr}(aC_3 + b)\left(\frac{c_1}{r_s}\ln\left(\frac{c_1}{r_s}\right) - \frac{c_1}{r_s} + 1\right) - \frac{aC_2\varepsilon_{cr}r_s}{4}\left(2\left(\frac{c_1}{r_s}\right)^2\ln\left(\frac{c_1}{r_s}\right) - \left(\frac{c_1}{r_s}\right)^2 + 1\right) \tag{2.34}$$

3 Discussion and experimental verification of confinement model

An estimate of the confining capacity found with the thick-walled-cylinder model given in Chapter 2 is shown in Fig. 3.1. The clamping action of the concrete is expressed by the radial compressive stress as a function of the radial strain at the interface, the latter being the radial displacement of the interface divided by the bar radius. The three stages mentioned in Chapter 2 are indicated. During stage I the cylinder remains uncracked and a liner elastic material behaviour is assumed. The transition into stage II is marked by the initiation of radial (macro)cracks starting at the interface. In this stage the cylinder is partly cracked and for the cracked part the softening of concrete in tension is taken into account. The penetration depth of the radial cracks is the control parameter in this stage. The maximum radial stress is reached after a penetration of about 70% of the cylinder wall. Further crack penetration results in a decrease of the radial stress, which is accelerated as soon as the entire cylinder wall is cracked. Then stage III begins, which is controlled by the radial crack width at the outer perimeter of the cylinder.

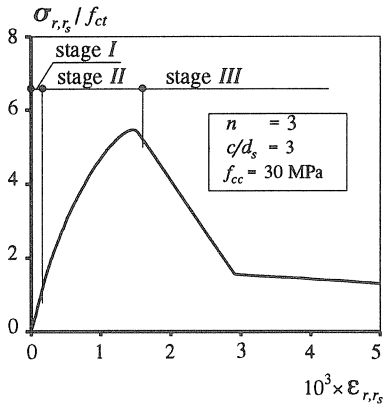

Fig. 3.1. Confining capacity estimated with the thick-walled-cylinder model (stage I: uncracked, stage II: partly cracked, stage III: entirely cracked).

A series of tests have been performed to verify and tune the confinement model. A conical steel bar (1:500 cone surface inclination; 12, 16 and 20 mm average diameter) with a smoothly grinded surface was embedded in a 25 mm thick concrete disc (80, 100, 120 and 140 mm diameter, 4 to 6 MPa splitting tensile strength). The bar was pulled through the disc measuring the pull-through force as a function of the free bar end displacement, thus obtaining a relationship between the average bond stress and the radial displacement of the interface. Under the assumption of a constant coefficient of friction this relationship is proportional to the radial stress versus radial strain relation found with the thick-walled-cylinder model. Some of the results are presented here.
In general 4 to 5 radial cracks started at the interface. In the beginning the penetration depth of all cracks was about the same, but at the end one of these cracks developed faster, clearly showing a

greater depth and a greater width. In the model, however, the cracks are supposed to open uniformly. To count for this discrepancy a smaller number of cracks is assumed in the model than observed in practice. As can be seen in Fig. 3.2, the choice of this parameter has a strong influence on the descending branch of the confining capacity curve. Good simulations have been obtained by fixing the number of cracks to three; see Fig. 3.3.

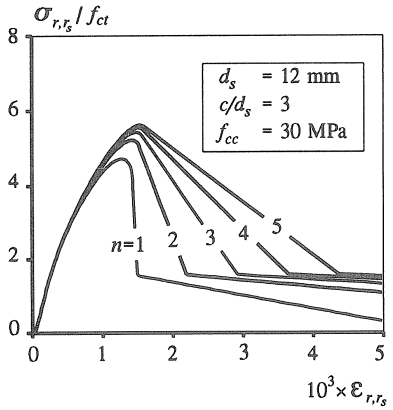

Fig. 3.2. Influence of assumed number of radial cracks on confinement capacity estimated with thick-walled-cylinder model.

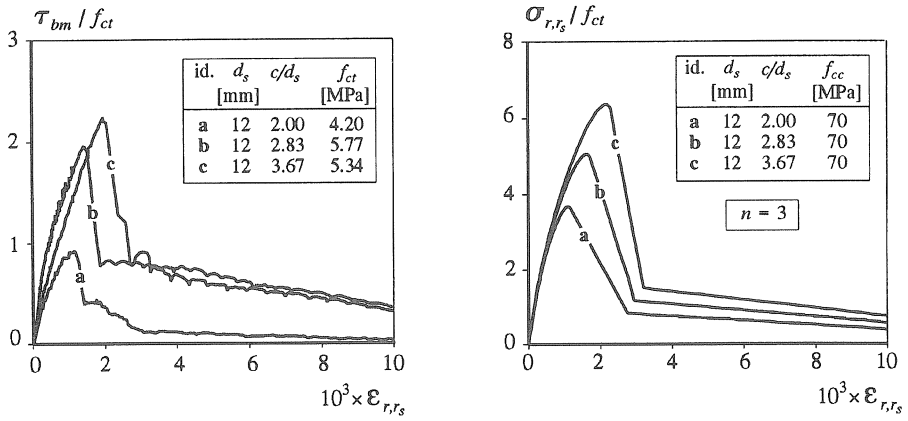

Fig. 3.3. Measured relation between bond stress and radial strain (left) and calculated relation between radial stress and radial strain (right).

The thick-walled-cylinder model is used to simulate the concrete clamping action on a reinforcing element. This requires a choice of the wall thickness that takes into account the real configuration with respect to cover and spacing. For this purpose an approach is presented in Section 4.3.2. Furthermore, bond conditions vary as a function of the bar position with respect to the bottom of the mould due to sedimentation of the fresh concrete. This aspect can be simulated by extending the

thick-walled-cylinder model with a thin boundary layer with a lower modulus of elasticity, see Den Uijl (1994).

4 Bond model

4.1 *Description of bond behaviour*

In this chapter a bond stress-slip relationship for a ribbed bar embedded in concrete is developed using the confinement model given in Chapter 2. For the evaluation of the bond strength a distinction is made between the splitting type and the pull-out type of bond failure, which are described in the following general description of the bond behaviour.

When bond between a ribbed bar and concrete is activated three consecutive stages of behaviour can be observed. First, the initial contact between steel and concrete is maintained by adhesion and interlocking of the cementitious matrix and the steel surface. In this stage an elastic bond behaviour is assumed, which is connected to small bond stress values. In the second stage, which starts when the initial bond is broken, bond is mainly governed by bearing of the ribs against the concrete. The concentrated bearing forces in front of the ribs cause the formation of cone-shaped cracks starting at the crest of the ribs. The resulting corbels between the ribs transfer the bearing forces into the surrounding concrete. In this stage the displacement of the bar with respect to the concrete (slip) consists of bending of the corbels and crushing of the concrete in front of the ribs, see Fig. 4.1 (Goto 1970). The bearing forces, that are inclined with respect to the bar axis, can be decomposed into the directions parallel and perpendicular to the bar axis. The parallel component equals the bond force, whereas the radial component induces circumferential tensile stresses in the surrounding concrete, which may result in radial cracks.

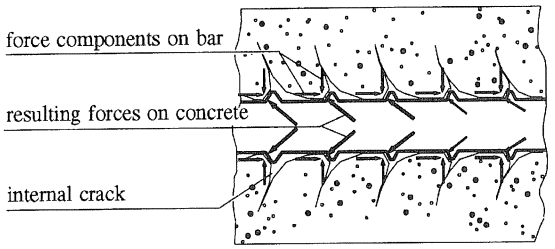

Fig. 4.1. Deformations around the bar for splitting bond failure, after Goto (1970).

Now two failure modes are to be considered. If the radial cracks propagate through the entire cover bond splitting failure is decisive. In that case the maximum bond stress follows from the maximum radial stress delivered by the surrounding concrete. Further crack propagation results in a decrease of the radial compressive stress. At reaching the outer surface – which marks the beginning of the third stage of the bond splitting failure mode – this stress strongly reduces resulting in a sudden

drop of the bond stress. Yet, the load bearing mechanism remains the same as in the previous stages.

When the confinement is sufficient to prevent splitting of the concrete cover bond failure is caused by pull-out of the bar. In that case a new sliding plane originates around the bar shearing off the concrete corbels and the force transfer mechanism changes from rib bearing into friction, see Fig. 4.2. The shear resistance of the corbels can be considered as a criterion for this transition, which in this case of pull-out bond failure mode marks the beginning of the third stage. Due to the lower roughness of the new sliding plane compared to that of the ribbed bar, the occurrence of this surface is connected with a considerable reduction of the radial compressive stress and, hence, with a reduction of the bond stress. Under continued loading the sliding surface is smoothened, due to wear and compaction, and the attendant volume reduction will result in release of the radial strain and in further reduction of the bond stress.

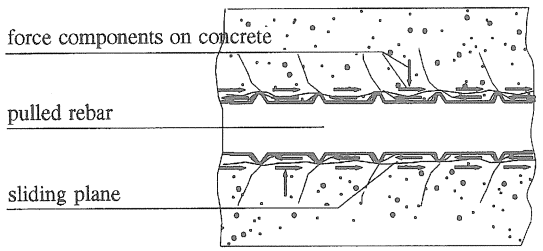

Fig. 4.2. Deformations around the bar for pull-out bond failure.

In general it is considered that the Poisson effect has a negligible influence on the bond resistance of ribbed bars. As long as rib bearing is the force transferring mechanism (splitting bond failure) this statement can be justified, considering that the transverse deformation connected to the local steel stress change is small compared to the rib height. However, when the force transfer mechanism changes from rib bearing to friction (pull-out failure) the local transverse deformation can not be disregarded considering the roughness of the sliding plane. In this case the Poisson effect may considerably influence the development of the radial compressive stress and, hence, the bond stress. For an increasing steel stress this will result in a release of the radial strain and, thus, in a reduction of the bond stress, which may become pronounced when the steel starts to yield.

4.2 *Modelling of bond behaviour*

4.2.1 Bond model formulation

To model the above described bond behaviour three steps are taken, see Fig. 4.3. Firstly, a boundary layer is assumed over which the localized displacements and forces acting at the interface are smeared out. The thickness of this boundary layer is disregarded so that the external diameter of the boundary cylinder equals the nominal bar diameter. Secondly, the ribbed bar is conceived as a conical bar, thus connecting the slip of the bar with the radial displacement of the interface. Finally, the bond mechanism is assumed to be based on dry friction, which makes the bond stress directly

proportional to the radial compressive stress. The relationship between the radial displacement and the radial compressive stress is given by the confinement model given in Chapter 2. It is noticed that in the confinement model the radial displacement of the interface is normalized to the bar radius, which results in a radial strain at the interface. From the radial compressive stress σ_r the bond stress τ_b is found by:

$$\tau_b = \sigma_r \cot(\theta) \tag{4.1}$$

with $\cot(\theta)$ coefficient of friction.

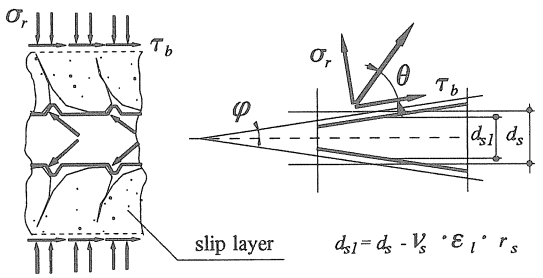

Fig. 4.3. Modelling steps.

The relationship between slip and radial displacement is given by the cone angle, thus representing the wedging action of the ribbed bar when displaced with respect to the surrounding concrete. This wedging action becomes active after the transition from adhesion to rib bearing, so with the beginning of the second stage. In the model the first stage, which comprises of adhesion and interlocking, is neglected.

In the third stage the cone angle depends on the failure mechanism. With bond splitting rib bearing continues to be the force transferring mechanism and in that case the cone angle remains the same. On the contrary, the development of the cylindrical sliding plane around the bar in the case of pull-out failure is connected with a much smaller roughness, which involves a reduction of the cone angle. Moreover, as the pull-out failure develops, the progressive smoothening of the sliding plane will cause a further reduction of the cone angle. It is assumed that this process is a function of the slip, and that the rate with which it occurs decreases as the slip increases. This holds also for the radial displacement of the interface, which reduces as the smoothening of the sliding plane continues.

These considerations result in different relationships between slip and radial strain for splitting failure and pull-out failure as shown in Fig. 4.4a and Fig. 4.4b, respectively. Furthermore, it can be seen that with increasing slip the entire confinement capacity curve is followed in the case of splitting failure, whereas in the case of pull-out failure only a part of the ascending branch of this curve is followed, first upward and then downward. The subscript *s* in Fig. 4.4b denotes the longitudinal steel strain and the influence of the Poisson effect on the radial strain. In fact, this influence is proportional to the change of the local steel strain. Assuming the initial value of the local steel strain to be zero, the change of the local steel strain corresponds to the local steel strain itself.

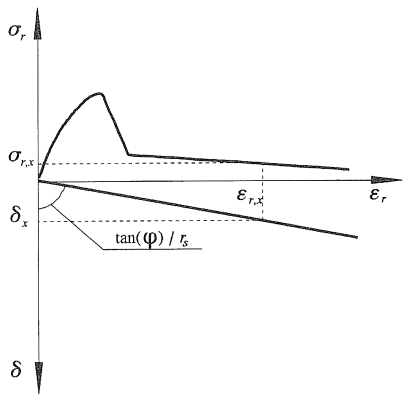

Fig. 4.4a. Relation between slip δ and radial stress σ_r for splitting bond failure.

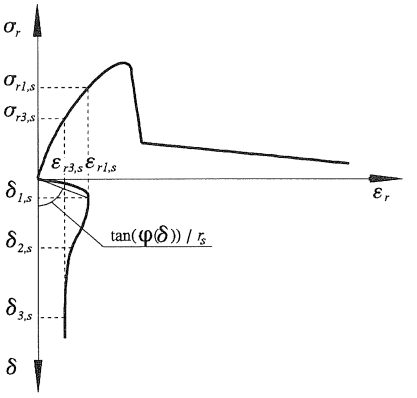

Fig. 4.4b. Relation between slip δ, steel strain ε_r and radial stress σ_r for pull-out bond failure.

For the mathematical formulation of the bond model a clear distinction is made between both bond failure modes: splitting and pull-out. For the splitting mode the most important influence is the wedging effect connected with the rib bearing mechanism. It has been argued that influence of the Poisson effect is small and therefore it is neglected. Wear and compaction do not play a role with this failure mode. Hence, for the splitting mode the radial displacement of the interface is expressed by:

$$\varepsilon_{r,r_s} = \delta \tan(\varphi) \tag{4.2}$$

with

δ = slip

φ = angle between cone surface and bar axis

For the pull-out mode of bond failure it has been reasoned that after the occurrence of the cylindrical sliding plane the cone angle diminishes as the slip increases, that the Poisson effect can not be disregarded and that wear and compaction of the sliding plane shall be taken into account. Thus in this case the radial displacement of the interface is influenced by a number of factors that can be connected with the slip and the local steel strain:

$$\varepsilon_{r,r_s} = \delta \tan(\varphi(\delta)) - \alpha_p \varepsilon_s \upsilon_s r_s - F(\delta) \tag{4.3}$$

with

$\varphi(\delta)$ = slip dependent cone angle

α_p = coefficient representing effectiveness of the release of the radial strain at the interface due to the bar contraction

ε_s = longitudinal steel strain in the bar

υ_s = Poisson constant of steel

$F(\delta)$ = slip dependent function representing the radial strain release due to the wear and compaction of the sliding plane

In absence of the information needed to quantify precisely all the above mentioned influences an expression is used that represents the combined influences of wedging, Poisson effect and wear of the sliding plane:

$$\varepsilon_{r,r_s} r_s = F_1(\delta, \varepsilon_s) \tag{4.4}$$

with $F_1(\delta, \varepsilon_s)$ being a function of the local slip and steel stress.

A graph described by this function for a constant steel strain ε_s is displayed in Fig. 4.5. It consists of three sections marked by the points a, b, c and d. The subscript *s* in the coordinates of these point refers to the steel strain. Section A and B are cubic parabolas, section C is an exponential function. In point b the tangent is horizontal, whereas c is a point of inflection. The coordinates of points b, c and d are derived from the position of the boundary curve shown with the dashed line, applying a reduction function, which implicitly takes into account the influences of the Poisson effect and of the sliding plane wear on the radial deformation. The coordinates of the boundary curve are discussed later. First, the expressions for the coordinates of the points a, b, c and d are given.

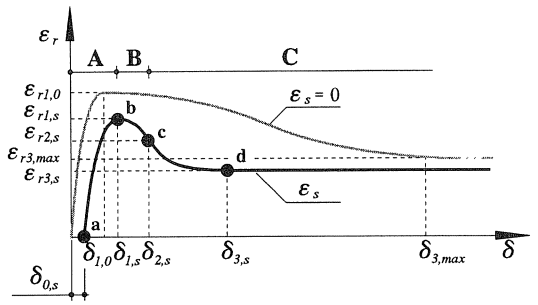

Fig. 4.5. Radial strain-slip relationship for pull-out bond failure.

The horizontal shift of point a is connected with the free space that occurs in front of a rib when only the Poisson effect is taken into account and no slip, see Fig. 4.6:

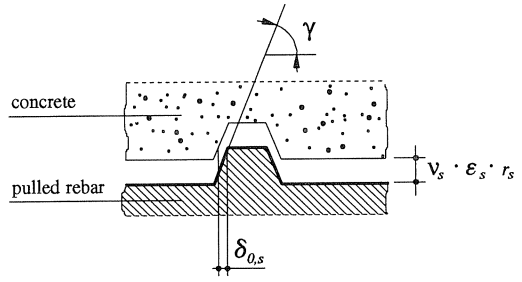

Fig. 4.6. Initial $\delta_{0,s}$ due to the bar contraction.

$$\delta_{0,s} = \frac{L_{ele}}{r_s}\frac{\upsilon_s \varepsilon_s r_s}{\tan(\gamma)} \tag{4.5}$$

with

L_{ele} = length of finite element
γ = rib face angle

The horizontal coordinate of point b equals::

$$\delta_{1,s} = \delta_{0,s} + \delta_{1,0} \tag{4.6}$$

The vertical coordinate of this point follows from:

$$\varepsilon_{r1,s} = (\varepsilon_{r1,0} - \varepsilon_{r3})e^{-K(\varepsilon_{r1})\varepsilon_s} + \varepsilon_{r3} \tag{4.7}$$

with $K(\varepsilon_{r1})$ a constant with which the reduction rate of ε_{r1} is controlled.
The coordinates of point c are arbitrarily chosen as follows:

The coordinates of point d are derived in a similar way as the vertical coordinate of

$$\delta_{2,s} = \frac{\delta_{3,s}}{2} \tag{4.8}$$

$$\varepsilon_{r2,s} = \frac{\varepsilon_{r1,s} + \varepsilon_{r3,s}}{2} \tag{4.9}$$

point b:

$$\delta_{3,s} = (\delta_{3,max} - \delta_{3,min})e^{-K(\delta_3)\varepsilon_s} + \delta_{3,min} \tag{4.10}$$

with $K(\delta_3)$ a constant with which the reduction rate of δ_3 is controlled.

$$\varepsilon_{r3,s} = (\varepsilon_{r3,max} - \varepsilon_{r3,min})e^{-K(\varepsilon_{r3})\varepsilon_s} + \varepsilon_{r3,min} \tag{4.11}$$

with $K(\varepsilon_{r3})$ a constant with which the reduction rate of ε_{r3} is controlled.

The boundary curve is derived on the basis of a number of assumptions and considerations, which are discussed hereafter. The criterion for the transition from the splitting failure mode into the pull-out failure mode is a critical bond stress $\tau_{b1,}$ which is assumed to be proportional to the tensile strength of the concrete. This bond stress is connected to a radial stress σ_{r1} according to eq. (4.1) and the radial strain $\varepsilon_{r1}(=\varepsilon_{r1,0})$ that corresponds to this radial stress is directly found from the confinement model; see Chapter 2. For the splitting failure mode the slip δ_1 connected to this radial strain is found with eq. (4.2). Considering that the transition from one failure mode into the other is

a gradual process, for pull-out failure this slip value is multiplied with an arbitrarily chosen value two:

$$\delta_{1,0} = 2\delta_1 = \frac{2\varepsilon_{r1,0}}{\tan(\varphi)} \tag{4.12}$$

The value of $\delta_{3,max}$ is put equal to the length of the concrete corbels between two subsequent ribs L_{key}, which value is proportional to the bar diameter, in general. The value of $\delta_{3,min}$ is arbitrarily put to 2.1 times $\delta_{1,0}$. The limit values of the radial strain, $\varepsilon_{3,max}$ and $\varepsilon_{3,min}$, are found from the assumed residual bond stress levels $\tau_{b3,max}$ and $\tau_{b3,min}$ after the slip induced strain release and the combined slip and steel stress induced strain release, respectively (conversion from bond stress to radial stress with eq. (4.1), and from radial stress to radial strain with confinement model; see Chapter 2).

4.2.2 Parameter choice

To calibrate the bond model and to set the values of model parameters, a number of calculations has been performed for various confinement and load arrangement conditions, as well as for concrete and steel with different material characteristics, see Section 4.4. Based on these comparative analyses the parameter values have been fixed as listed in the Table 4.1.

Table 4.1 Bond model parameters.

notation	parameter name	value/expression	remarks
$\cot(\theta)$	coefficient of friction	1	constant
φ	cone angle [deg]	$0.1 \times f_c$	concrete strength dependent
γ	rib face angle	60°	bar geometry dependent
$K(\varepsilon_{r1})$	constant for reduction of ε_{r1}	30	constant
$K(\varepsilon_{r3})$	constant for reduction of ε_{r3}	8.5	constant
$K(\delta_3)$	constant for reduction of δ_3	100	constant
τ_{b1}	critical bond stress	$5 \times f_{ct}$	concrete strength dependent
$\tau_{b3,max}$	max. residuel bond stress	$2.5 \times f_{ct}$	concrete strength dependent
$\tau_{b3,min}$	min. residual bond stress	0	constant
$\delta_{3,max}$	characteristic slip value	$L_{key} = 0.33 \times d_s$	bar geometry dependent

Besides the model parameters, also material characteristics of reinforcing steel and concrete are the input data of the proposed bond model. It should be remarked in this respect that to describe the properties of concrete a fracture mechanics approach is used, see Chapter 2.

4.3 Structural modelling

4.3.1 Load introduction zone

The local bond stress-slip response is affected by the state of stress in the surrounding concrete. Since this state of stress significantly differs with different loading and boundary conditions, it is not surprising that differences in bond stress-slip relations along the transmission length of an embedded bar can occur.

In the bond model described in Section 4.2 the local bond stress is conceived as being based upon the response of concrete disc surrounding the bar at that particular position. This is a simplification of reality, for the rib bearing forces are spread into the concrete under a certain angle, thus also activating the concrete in adjacent concrete discs. This "linkage effect" shall be taken into account since it may result in significant differences in bond strength and stiffness, depending on the degree of restraint near the end of a concrete member or near a crack, and on the direction of bar movement with respect to the entrance plane. This has experimentally been shown by Cowell et al. (1982) in the case of pull-out and push-in tests.

Pull-out loading with relative displacement into the direction of the free edge will result in an earlier occurrence of radial cracks due to lack of restraint. In those cases often a concrete cone is pulled out. Both the occurrence of the radial cracks and the cone pull-out are connected with a considerable reduction of the bond stress and this effect is often taken into account by assuming a bond free length of $2d_s$; e.g. König and Fehling (1988). In the present model a more refined approach is used, however. To count for the influences related to the introduction of bond forces near the entrance plane it is assumed that the force is spread out in a conical volume. Hence, the activated concrete area is proportional to the distance from the entrance plane. The angle ψ between the axis and the surface of the cone depends on the direction of the slip with respect to the entrance plane and the confining conditions near the entrance plane. When the bar moves from the entrance plane, the angle ψ is put equal to 90°, which means that the bond stresse are not reduced. For the opposite direction of relative bar movement the angle ψ varies from 40° when the entrance plane coincides with a free edge, such as a crack, to 90° when the entrance plane is restraint, such as in pull-out tests with a bond free zone.

4.3.2 Effective concrete cover

The present bond model for ribbed bars is based on the confinement delivered by the surrounding concrete. The bond force is limited by the maximum radial component that can be equilibrated by the radial compressive stresses resulting from the concrete confinement. After the occurrence of radial cracks a redistribution of the internal stresses may take place due to local changes in stiffness. The internal stress distribution around a bar will strongly depend on the geometry of the member cross section and the position of the reinforcing bars.

It has been observed in experiments with equal bottom cover that both the crack pattern around a bar and the ultimate resistance against splitting are influenced by other cross-sectional dimensions (Morita et al. 1994, Den Uijl 1992). This observation supports the supposition that the confinement delivered by the concrete not only depends on the smallest concrete cover, but that a greater part of the concrete cross-section may contribute to it as well. This is taken into account by considering an effective concrete cover on the bar, which is related to the dimensions of the concrete cross section and the lay-out of the reinforcing elements. This effective concrete cover – as it is mentioned hereafter – is used to simulate the confinement conditions of the considered bar by means of the thick-walled cylinder model. The following expression has been chosen:

$$c_{\mathrm{eff}} = \frac{1}{m}\sum_{i=1}^{m}[c_i\chi(c_i) + c_{\mathrm{eff,max}}(1-\chi(c_i))] \tag{4.13}$$

with

c_{eff} = effective concrete cover

$c_{eff,max}$ = maximum effective concrete cover to be taken into account

m = number (3 or 4) of equally spaced directions to be taken into account depending on section geometry

c_i = cover thickness in each of m directions

$\chi(c_i)$ = indicator function, defined as follows:

$\chi(c_i) = 1$ if $c_i \leq c_{eff,max}$

$\chi(c_i) = 0$ if $c_i > c_{eff,max}$

The maximum effective concrete cover is defined as the length of the most probable splitting crack:

$$c_{eff,max} = \frac{c_{i,min} + r_s}{\cos(\alpha)} - r_s \tag{4.14}$$

with

$c_{i,min}$ = smallest concrete cover to be taken into account

α = angle between critical splitting plane and normal to closest concrete surface ($\alpha = 45$–$60°$)

If more than one bar is located in a section a fictitious cover of $0.75s_i$ is assumed, s_i being the clear bar spacing in the direction considered. This assumption takes into account that the concrete in between the bars is more effective in resisting the circumferential tensile stresses than the concrete in the cover, for the stress distribution is more uniform in the former case. In Fig. 4.7 some examples of effective concrete cover for bars in members with different geometries are given.

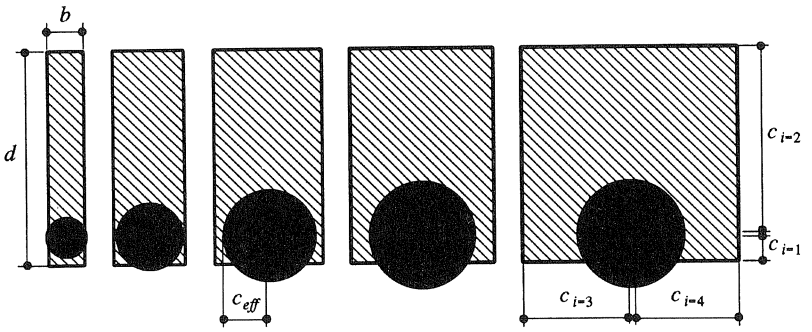

Fig. 4.7. Effective concrete cover for different member geometry.

4.3.3 Additional confinement

Among the parameters affecting bond efficiency the confinement plays a major role. When analyzing the behaviour of a structure it shall be considered whether, besides the clamping action of the concrete surrounding the bar, also additional confinement is available. This can be the active confinement resulting from loads transverse to the bar, i.e. resulting from a support or from the column force in a beam-column joint, or passive confinement delivered by transverse reinforcement. In practice often both active and passive confinement will be present.

The active confinement is more efficient than the passive one, since its effect does not depend on the mobilized bond stress. Passive confinement, on the contrary, depends on concrete dilatancy connected to the radial stress at the concrete-to-steel interface. Furthermore, the influence of additional confinement depends on the bond failure mode. Maeda et al. (1995) observed an increase of bond strength proportional to the confining stress delivered by the transverse reinforcement in case of bond splitting failure. As far as the pull-out failure is concerned it is usually assumed that once the transition from rib bearing to friction has taken place the bond strength can not be increased by transverse reinforcement (Eligehausen et al. 1983). On the contrary, active confinement will contribute to the bond strength in both failure modes (Eligehausen et al. 1983; Malvar 1992). It is reported that tensile stresses perpendicular to the bar may result in a negative contribution to the confinement (Nagatomo 1992). Although the present confinement model given in Chapter 2 only deals with the clamping action of the concrete surrounding the bar it seems feasible to include the passive and active confinement as well.

4.4 *Bond model verification*

The validity of this concrete confinement based bond model has been verified by comparing model predictions with results of tests, where well defined confinement conditions had been created. By this means also the potentials of the model, further discussed in Bigaj et al. (1996), have been shown.

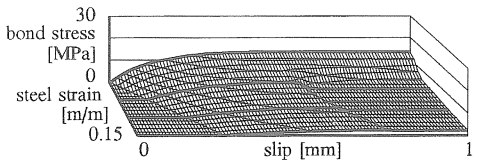

Fig. 4.8a. Bond stress-slip relationships for pull-out bond failure for NSC *(steel strain dependence shown).*

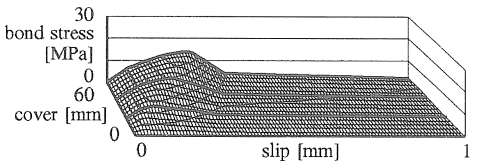

Fig. 4.8b. Bond stress-slip relationships for splitting bond failure for NSC *(concrete cover effect shown).*

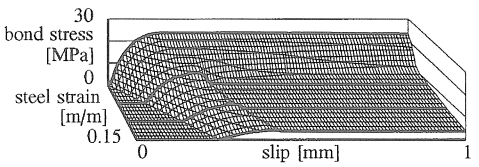

Fig. 4.8c. Bond stress-slip relationships for pull-out bond failure for HSC.

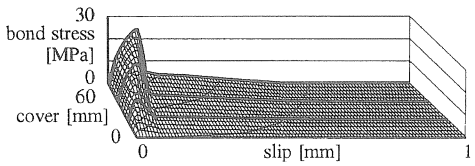

Fig. 4.8d. Bond stress-slip relationships for splitting bond failure for HSC.

In this model the capacity of the concrete cover to resist radial compressive stresses has not only a decisive influence on the ultimate bond resistance, but it also controls the simulation of the bond failure mode. The model is capable of representing bond behaviour for both modes of bond failure: splitting and pull-out.

Owing to the implementation of the fracture mechanics based description of the concrete behaviour, the bond properties of concrete with different strength and toughness can properly be estimated. Fig. 4.8a-d show the examples of bond stress-slip relationships obtained for both bond failures for two types of concrete, namely normal strength concrete (NSC) with a cubecompressive strength f_{cc} = 35 MPa and for high strength concrete (HSC) with a cube compressive strength f_{cc} = 107 MPa (bar diameter d_s = 20mm; some specific curves highlighted). Experimentally observed significant differences in the bond behaviour of HSC and NSC clearly appear when corresponding diagrams are compared (Fig. 4.8a and 4.8c for pull-out mode of bond failure, Fig. 4.8b and 4.8d for splitting mode of bond failure).

The model enables the prediction of the actual bond stress-slip relationship for a particular load path (the steel stress-strain characteristics dependence included) and for particular geometrical characteristics of the specimen (the confinement and boundary conditions dependence involved).

In order to demonstrate the ability of the model to simulate the bond resistance in a wide range of steel deformations the calculated results are compared with those obtained in pull-out tests with long embedment lengths (Bigaj, 1995), as shown in Fig. 4.9 and 4.10. In both figures, additionally to the test simulation curves, the simulations valid for various constant values of steel strain levels ε_s are shown. It must be remembered that during the tests the steel strain does not remain constant but changes from $\varepsilon_s = 0$ to $\varepsilon_s = \varepsilon_{su}$, where ε_{su} is the ultimate steel strain. An equally good agreement is found for test series with HSC and NSC – both concerning the steel stress and slip development along the transmission length and the bond stress-slip relationships.

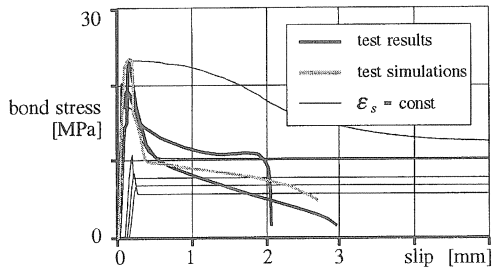

Fig. 4.9. Comparison of test results and test simulations for long embedment length – HSC *(Bigaj, 1995)*

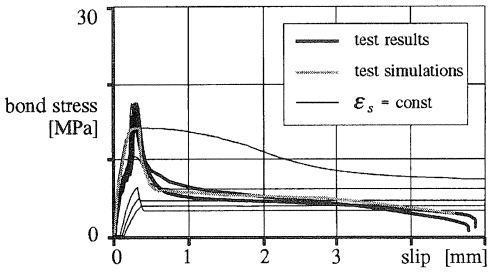

Fig. 4.10. Comparison of test results and test simulations for long embedment length – HSC (Bigaj, 1995).

This holds for other load arrangements and boundary conditions as well – besides the beam bending tests (Bigaj, 1996), the experiments (Manfredi and Pecce, 1996), where conditions as between two cracks have been created and the bond behaviour in the post-yield range of steel deformations has been studied (short embedment length, zero slip values with non-zero steel stress value), were simulated with very good agreement, see Fig. 4.11. In modelling of all these cases the discussed above assumptions concerning the load introduction zone and the effective concrete cover have been involved.

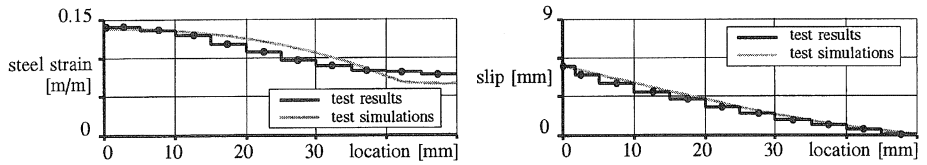

Fig. 4.11. Comparison of test results and test simulations for short embedment length (Manfredi and Pecce, 1996).

The potentials of the model to simulate the effect of reinforcing steel characteristics on the bond stress-slip relationships could be proven by comparison with test results (Shima et al. 1987), where this effect has been studied in pull-out tests with long embedment lengths, see Fig. 4.12. It shows that the model accounts in a proper manner for the influence of reinforcing steel deformation on the bond strength development.

With regard to the bar size, the discussed model is capable of representing the bar size effect on the bond behaviour. This influence is implicitly included, owing to the fracture mechanics based description of the splitting crack propagation process. There is not so much experimental evidence available concerning this phenomenon, since most of the tests have been performed with only one bar size at the time, or the bar size variation has been very limited. Some more extensive research (Morita et al., 1994) confirms, however, that the bar size effect on the bond behaviour exists. They found a change in the rate of bond strength decrease with increase of the bar diameter for a changing concrete cover thickness. They also reported the bar size insensitivity of the ultimate bond stress in cases where pull-out type of bond failure takes place. In Fig. 4.13, where the simulations with the concrete confinement based bond model are shown, the same tendencies are observed.

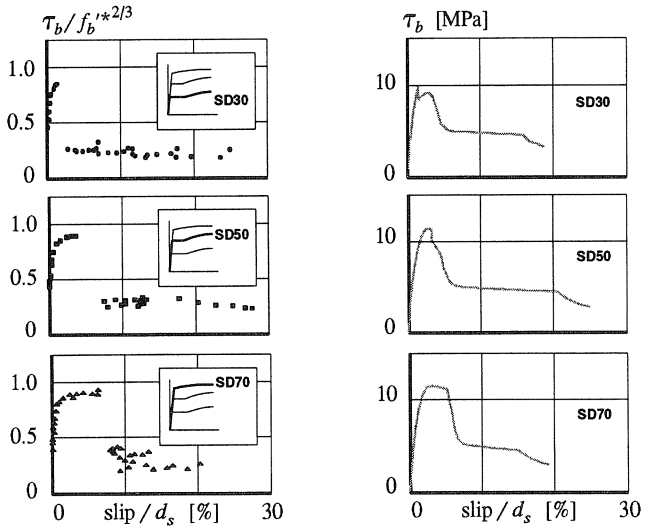

Fig. 4.12. Effect of reinforcing steel characteristics on bond stress-slip relationship comparison of test results (left column) and test simulations (right column) (Shima et al., 1987).

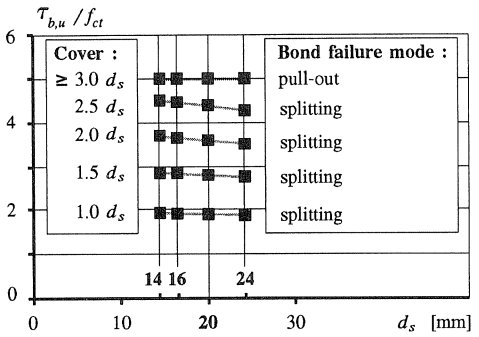

Fig. 4.13. Bar size effect on ultimate bond strength.

5 Concluding remarks

Based on experimental and analytical studies a bond model for ribbed bars has been developed. In this model the concrete confining capacity is used as a starting point. The model is capable of predicting the response of materials with various fracture properties, such as NSC and HSC, both for splitting and pull-out type of bond failure. In this way the significant differences in the bond behaviour of HSC and NSC can be studied and the bond resistance of any concrete type in any confinement conditions can be predicted. The model accounts for the effect of bar deformation on the bond stress-slip relationship, also in the post-yield range. These characteristics make this bond model a

suitable tool in analyzing the behaviour of structural members in the serviceability as well as in the ultimate limit state, i.e. in studying problems such as deformation capacity of reinforced concrete structures.

6 Acknowledgement

This investigation has financially been supported by the Dutch Foundation for Technical Sciences (STW) under grant DCT 22.2774.

7 Symbols

a constant, see eq. (2.8)
b constant, see eq. (2.8)
c clear concrete cover
c_1 clear concrete cover plus bar radius
c_{cr} wall thickness of cracked part of cylinder
c_{eff} effective concrete cover = wall thickness of cylinder
$\cot(\phi)$ coefficient of friction
d_s bar diameter
f_c concrete cylinder compressive strength
f_{cc} concrete cube compressive strength
f_{ct} concrete tensile strength
l_{ch} characteristic length
n number of radial cracks
r radius
r_{cr} radius of crack front
r_e radius of cylinder outer face
r_i radius of cylinder inner face
r_s bar radius
$u_{r,ri}$ radial displacement of cylinder inner face
w_0 fictitious crack width at which no stress is transferred
w_t fictitious crack width at which tensile stress σ_t is transferred

C_1 constant, see eq. (2.4)
C_2 constant, see eq. (2.17)
C_3 constant, see eq. (2.29)
E_c elastic modulus of concrete
G_f fracture energy

α constant, see Fig. 2.2
β constant, see Fig. 2.2

δ slip

$\Delta_{t,r}$ elongation of circumferential fibre with radius r

Δ_{tot} constant elongation of circumferential fibres across the cylinder wall

ε_{cr} concrete strain for $\sigma_t = f_{ct}$

ε_s steel strain

$\varepsilon_{t,r}$ tangential strain in circumferential fibre with radius r

φ angle between cone surface and bar axis

υ_c Poisson constant of concrete

$\sigma_{r,r}$ radial stress at radius r

σ_t tensile stress

$\sigma_{t,r}$ tangential stress at radius r

τ_b bond stress

superscripts

LE linear elastic; refers to contribution of uncracked part of the cylinder

NL non linear; refers to contribution of cracked part of the cylinder

I uncracked stage of behaviour

II partly cracked stage of behaviour

III entirely cracked stage of behaviour

RBM rigid body movement

Δc change of wall thickness

8 References

BIGAJ A.J.(1995), Bond behaviour of deformed bars in NSC and HSC. Stevin Report 25.5-95-II. TU Delft, pp. 132.

BIGAJ A.J., WALRAVEN J.C. (1996), Modelling of size effect on rotation capacity of plastic hinges in reinforced concrete members. Proceedings of AIO-Congress 1996 "From materials to Building Structures". Onderzoekschool Bouw, pp. 12.

BIGAJ A.J., DEN UIJL J.A., WALRAVEN J.C. (1996), A bond model for ribbed bars in HSC and NSC – an experimental study. Proceedings of 4th International Symposium on Utilization of High-strength/High-performance Concrete. Paris, pp. 1125-1134.

BIGAJ A.J. (to be published in 1996), Bond behaviour of deformed bars in NSC and HSC – part II. Stevin Report. TU Delft.

CEB-FIP Model Code 1990 for Concrete Structures (1991). CEB Bulletin d'Information No. 228, pp. 205.

COWELL A.D., POPOV E.P., BERTERO V.V. (1982), Effects of concrete types and loading conditions on local bond-slip relationships. Report No. UCB/EERC 82/17. Earthquake Engineering Research Centre. University of California, Berkeley, pp. 62.

DEN UIJL J.A. (1992a), Bond and splitting action of prestressing strand. Proceedings of the International Conference on Bond in Concrete. Riga, pp. 2.79–2.87.

DEN UIJL J.A. (1992b), Background of the CEB-FIP Model Code 90 clauses on anchorage and transverse tensile actions in the anchorage zone of prestressed concrete members. CEB Bulletin d'Information No. 212, pp. 71–94.

DEN UIJL J.A. (1994), Das Verhalten von Spannlitzen im Rahmen der Bruchmechanik. Deutscher Ausschuss für Stahlbeton. Beiträge zum 29. Forschungskolloquium am 24. und 25 März an der TU Delft, pp. 81–88.

ELIGEHAUSEN R., POPOV E.P. BERTERO V.V. (1983), Local bond stress-slip relationships of deformed bars under generalized excitations. Report No.UCB/EERC 83/23. Earthquake Engineering Research Centre. University of California, Berkeley, pp. 169.

GOTO Y. (1970), Cracks formed in concrete around deformed tension bars. Journal of the American Concrete Institute. Proceedings Vol. 68, No. 4, pp. 241–251.

HILLERBORG A. (1983), Analysis of one single crack. Fracture Mechanics of Concrete. Ed. F.H. Wittmann. Elsevier, pp. 223–249.

KÖNIG G., FEHLING E. (1988), Zur Rissbreitenbeschränkung in Stahlbetonbau. Beton und Stahlbetonbau 83, H6.

MAEDA M., OTANI S., AOYAMA H. (1995), Effect of confinement on bond splitting behaviour in reinforced concrete beams. Structural Engineering International 3/95, pp. 166–171.

MALVAR J.L. (1992). Confinement stress dependent bond behaviour. Proceedings of the International Conference on Bond in Concrete. Riga, pp. 1.79–1.88.

MANFREDI G. and PECCE M. (to be published in 1996), Bond behaviour between concrete and steel in large post-yield field. Journal of Mechanics and Structures, pp. 21.

MORITA S., FUJI S. (1982), Bond capacity of deformed bars due to splitting of surrounding concrete. Proceedings of International Conference on Bond in Concrete. Paisley College. Scotland, pp. 331–341.

MORITA S., FUJI S., KONDO G. (1994), Experimental study of size effect in concrete structures. Proceedings of JCI International Workshop on Size Effect in Concrete Structures, pp. 27–46.

NAGATOMO K., KAKU T. (1992), Bond behaviour of deformed bars under lateral compressive and tensile stress. Proceedings of the International Conference on Bond in Concrete. Riga, pp. 1.69–1.78.

ROELFSTRA P.E., WITTMANN F.H. (1986), Numerical method to link strain softening with failure of concrete. Fracture Toughness and Fracture Energy of Concrete. Ed. F.H. Wittmann, Elsevier, pp. 163–175.

SCHLAICH J., SCHÄFER K. (1991), Design and detailing of structural concrete using strut-and-tie models. The Structural Engineer, Vol. 69, No. 6.

SHIMA H., CHOU L.L., OKAMURA H. (1987), Bond characteristics in post-yield range of deformed bars. Concrete Library of JSCE No.10, pp. 113–124.

TEPFERS R. (1979), Cracking of concrete cover along anchored deformed reinforcing bars. Magazine of Concrete Research Vol. 31. No. 106, pp. 3–12.

TIMOSHENKO S. (1976), Strength of materials. Part II. Advanced Theory and Problems. Van Nostrand Reinhold, pp. 205-210.

VAN DER VEEN C. (1990), Theoretical and experimental determination of crack width in reinforced concrete at very low temperatures. Heron Vol. 35, No. 2, pp. 104.

WALRAVEN J.C., HAN N., STROBAND J. (1993), Experimenteel onderzoek aan beton met hoge sterkte. CUR-Commissie Rapport 93-7 Part II (in Dutch), pp. 38–75.